Inorg. Chem. **1989**, *28*, 3249-3258 **3249**

Contribution from the Institut für Anorganische Chemie, Universität Bern, CH-3000 Bern 9, Switzerland,
Institut für Anorganische Chemie, Universität Hannover, D-3000 Hannover 1, Federal Republic of Germany,
and Institut de Chimie Inorganique, Université de Fribourg, CH-1700 Fribourg, Switzerland

Optical Spectroscopic and Structural Properties of V^{3+}-Doped Fluoride, Chloride, and Bromide Elpasolite Lattices

Christian Reber,[1a] Hans U. Güdel,*[,1a] Gerd Meyer,[1b] Thomas Schleid,[1b] and Claude A. Daul[1c]

Received February 8, 1989

The crystal structures of the following seven elpasolites were determined by X-ray diffraction: K_2NaScF_6 (a = 8.4717 (5) Å), Cs_2LiYCl_6 (a = 10.4857 (5) Å), Cs_2NaYCl_6 (a = 10.7396 (7) Å), and Cs_2NaYBr_6 (a = 11.3047 (6) Å) crystallize in the cubic space group $Fm3m$. $Cs_2LiScBr_6$ crystallizes in the so-called 2L-type lattice, space group $P\bar{3}m1$, with lattice constants a = 7.611 (1) Å and c = 6.502 (1) Å. $Cs_2LiScCl_6$ and $Cs_2LiInCl_6$ both crystallize in the 12L-type lattice, space group $R\bar{3}m$, with lattice constants a = 7.2965 (6), c = 35.989 (4) Å and a = 7.3184 (4), c = 36.240 (3) Å, respectively. There are two inequivalent Sc^{3+} and In^{3+} sites, respectively. Single-crystal luminescence and absorption spectra of V^{3+} doped in fluoride, chloride, and bromide elpasolites are presented. Sharp, structured near-infrared luminescence is observed from all the lattices at temperatures below 20 K. The luminescence decay times are between 1.5 and 26 ms for the various lattices in this temperature range. For the cubic elpasolite K_2NaScF_6 and the hexagonal lattices $Cs_2LiScCl_6$, $Cs_2LiInCl_6$, and $Cs_2LiScBr_6$, the luminescence fine structure can be correlated with the crystal structure. Two inequivalent sites for V^{3+} are spectroscopically distinguishable in $Cs_2LiScCl_6$ and $Cs_2LiInCl_6$ in agreement with the X-ray diffraction results. Electronic and vibronic splittings of the ${}^3T_{1g}{}^a$ (O_h notation) ground state are directly obtained from these luminescence spectra. Observed electronic transition energies are compared with the results of crystal-field calculations. Broad-band luminescence with decay times between 120 and 380 μs arises with increasing temperature in all the chloride and bromide lattices and dominates the spectra between 200 and 300 K. This effect reflects the change of the emitting state from ${}^1T_{2g}$ at low temperature to the thermally populated ${}^3T_{2g}$ state at high temperature. A simple radiative relaxation model that takes into account both these excited states is presented and applied to the observed temperature-dependent decay times.

1. Introduction

The optical spectroscopic and especially the luminescence properties of V^{3+} have not received much interest in the past, in contrast to other first-row transition-metal ions that luminesce in the visible spectral range, such as Cr^{3+} or Mn^{2+}.[2] The V^{3+} luminescence lies in the near-infrared (near-IR) region, beyond the range of photomultipliers, and is thus less easily accessible. The only systems from which V^{3+} luminescence was observed so far are $Al_2O_3{:}V^{3+}$,[3] $Y_3Al_5O_{12}{:}V^{3+}$,[4] and $V(urea)_6(ClO_4)_3$.[5] We recently started to investigate the luminescence properties of halide lattices doped with V^{3+}[6] and the isoelectronic Ti^{2+}.[7] Intense emission spectra with sharp structure and luminescence decay times in the millisecond range were obtained from these systems at low temperatures, providing very nice examples of high-resolution near-IR luminescence spectra.

In the present work we use the chemical composition and the V^{3+} site symmetry of the host lattice as experimental variables to study the development of both the luminescence spectra and the decay behavior. For this purpose we have prepared a variety of V^{3+}-doped fluoride, chloride, and bromide elpasolites A_2BMX_6 (A = K, Rb, Cs; B = Li, Na; M = Sc, In, Y; X = F, Cl, Br). It is the first time that such a broad range of related elpasolite lattices doped with one transition-metal ion is investigated in a comparative study. These lattices have cubic, tetragonal, or hexagonal crystal structures,[8-10] offering a variety of structurally different lattice sites for V^{3+}. Some of these lattices provide two crystallographically inequivalent trivalent sites for V^{3+}, a very attractive prospect for high-resolution laser spectroscopy with its potential for a selective study of the individual species. Knowledge of the exact MX_6 geometry of the host lattices is essential for a correlation of structural and luminescence properties. The structures were therefore determined by X-ray diffraction, and the results are summarized in section 3.1.

V^{3+}, belonging to the $(3d)^2$ electron configuration, has a ${}^3T_{1g}$ ground state, which may be split by spin-orbit coupling and noncubic crystal-field components. In the excited state we are close to the crossover point of ${}^1T_{2g}$ and ${}^3T_{2g}$. In the cubic elpasolite lattices Cs_2NaYCl_6 and Cs_2NaYBr_6, which were studied spectroscopically and reported before,[6] the V^{3+} luminescence was found to originate in ${}^1T_{2g}$ and ${}^3T_{2g}$, respectively. This crossover region is particularly interesting, because the luminescence properties are expected to be strongly dependent on chemical and structural variations. Quite dramatic differences in the nonradiative relaxation behavior of V^{3+} were found in the series of host lattices investigated here.[11] The ${}^1T_{2g} \rightarrow {}^3T_{1g}{}^a$ transition, which is an intraconfigurational $(t_{2g})^2$ transition in the strong-field approximation, is expected to yield sharp luminescence lines. This is indeed the case, and the spectra have a very high information content. For their measurement, however, we have to push the instrumental resolution to the limit, which is only possible with the most sensitive Ge detectors covering the principal range of V^{3+} emissions between 1000 and 1600 nm very nicely. Electronic splittings of the ${}^3T_{1g}{}^a$ ground state and vibronic effects are responsible for the rich fine structure observed in our low-temperature luminescence spectra. The electronic splittings are correlated with the VX_6 coordination geometries and rationalized by crystal-field calculations. Variations of crystal field and electron repulsion parameters can be interpreted in terms of the spectrochemical and nephelauxetic series.

There is a strong current interest in the synthesis and development of new compounds that show near-IR luminescence. There are possible applications of such materials as solid-state lasers or solar concentrators. Several 3d transition-metal ions as e.g. Cr^{3+}, V^{2+}, Ni^{2+}, and Co^{3+} have received considerable attention in this respect.[12] The two $(3d)^2$ ions V^{3+} and Ti^{2+}, on the other hand, have been neglected. The present contribution provides some insight into the luminescence and excited-state relaxation properties of V^{3+}, which may help in the design and synthesis of new luminescent materials.

2. Experimental Section

The V^{3+}-doped chloride and bromide elpasolites were prepared as described in the literature.[6,8,9,13] Single crystals were grown in quartz

---

(1) (a) Universität Bern. (b) Universität Hannover. (c) Université de Fribourg.

(2) Luminescence of Inorganic Solids; Di Bartolo, B., Ed.; Plenum Press: New York, 1978.

(3) Goldschmidt, Z.; Low, W.; Foguel, M. *Phys. Lett.* **1965**, *19*, 17.

(4) Weber, M. J.; Riseberg, L. A. *J. Chem. Phys.* **1971**, *55*, 2032.

(5) Flint, C. D.; Greenough, P. *Chem. Phys. Lett.* **1972**, *16*, 369.

(6) Reber, Ch.; Güdel, H. U. *J. Lumin.* **1988**, *42*, 1.

(7) Jacobsen, S. M.; Güdel, H. U.; Daul, C. A. *J. Am. Chem. Soc.* **1988**, *110*, 7610.

(8) Meyer, G.; Dietzel, E. *Rev. Chim. Miner.* **1979**, *16*, 189.

(9) Meyer, G.; Gaebell, H.-C. *Z. Naturforsch.* **1978**, *33B*, 1476.

(10) Meyer, G. *Prog. Solid State Chem.* **1982**, *14*, 141.

(11) Reber, Ch.; Güdel, H. U. Submitted for publication.

(12) *Spectroscopy of Solid-State Laser Type Materials*; Di Bartolo, B., Ed.; Plenum Press: New York, 1987.

0020-1669/89/1328-3249$01.50/0

Table I. Structure Refinements of the Four Cubic Elpasolites K_2NaScF_6, Cs_2LiYCl_6, Cs_2NaYCl_6, and Cs_2NaYBr_6

crystal system cubic; space group $Fm3m$ (No. 225); $Z = 4$

data collection: four-circle diffractometer Siemens-Stoe AED 2, Mo Kα radiation, graphite monochromator, $\lambda = 0.7107$ Å, ω-scan; scan speed and width: variable, $3° \leq \theta \leq 30°$

data corrections: background, polarization and Lorentz factors; absorption: ψ-scan for 10 reflections

structure determination/refinement: program system SHEL-X76,[a] structure factors from Cromer et al.,[b] initial atomic positions from K_2NaAlF_6[c] (except for Cl, from difference Fourier syntheses), full-matrix least-squares refinement, $w = k[\sigma(F_o)^{-2}]$

Atomic Positions

A_2BMX_6		x/a	y/b	z/c	temp factors
A	8c	0.25	0.25	0.25	$U_{11} = U_{22} = U_{33}$; $U_{23} = U_{13} = U_{12} = 0$
B	4b	0.5	0.5	0.5	
M	4a	0	0	0	
X	24e	x	0	0	U_{11}; $U_{22} = U_{33}$; $U_{23} = U_{13} = U_{12} = 0$

Crystallographic Data

	K_2NaScF_6	Cs_2LiYCl_6	Cs_2NaYCl_6	Cs_2NaYBr_6
a/Å	8.4717 (5)	10.4857 (5)	10.7396 (7)	11.3047 (6)
$F(000)$	472	992	1024	1456
μ/cm^{-1}	25.16	120.64	113.12	250.01
no. of refl	98	113	108	114
R	0.043	0.013	0.041	0.059
R_w	0.044	0.012	0.019	0.027
k	0.859	1.597	1.105	1.887
x/a(X)	0.2342 (5)	0.25046 (9)	0.2439 (3)	0.2446 (2)
U_{11}(A)/Å^2	0.0273 (6)	0.0263 (2)	0.0345 (3)	0.0415 (5)
U_{11}(B)/Å^2	0.0133 (10)	0.0454 (60)	0.0370 (39)	0.0496 (75)
U_{11}(M)/Å^2	0.0081 (4)	0.0129 (2)	0.0119 (6)	0.0109 (9)
U_{11}(X)/Å^2	0.0137 (19)	0.0128 (5)	0.0157 (11)	0.0174 (9)
U_{22}(X)/Å^2	0.0664 (23)	0.0300 (4)	0.0496 (8)	0.0660 (7)
d(M–X), 6×/Å	1.984	2.626	2.619	2.765
d(A–X), 12×/Å	2.998	3.707	3.798	3.997
d(B–X), 6×/Å	2.252	2.617	2.750	2.887
d(X–X), 4×/Å	2.806	3.700	3.704	3.910
d(X–X), 4×/Å	3.184	3.714	3.890	4.083

[a] Reference 18. [b] Reference 19. [c] Reference 20.

ampules from the melt with the Bridgman technique. For the fluoride elpasolite K_2NaScF_6:V^{3+}, $K_2NaScCl_6$ was first prepared in analogy to the route described in ref 13. The chloride was then reacted with elemental fluorine at about 300 °C in an open crucible, yielding K_2NaScF_6. V^{3+} was added as K_2NaVF_6, synthesized according to

$$2KF + NaF + V + \tfrac{3}{2}CuF_2 \rightarrow K_2NaVF_6 + \tfrac{3}{2}Cu \qquad (1)$$

in a sealed tantalum ampule where copper reacts with the tantalum wall. Single-crystal growth of K_2NaScF_6:V^{3+} was then achieved from such a mixture by the Bridgman technique in a sealed tantalum ampule that had been jacketed in a quartz ampule with a furnace temperature of 1010 °C.[14] All crystals were checked for purity by X-ray powder diffraction.

Crystals suitable for single-crystal X-ray structure determination of Cs_2LiYCl_6, Cs_2NaYCl_6, Cs_2NaYBr_6, K_2NaScF_6 (all cubic, see Table I), $Cs_2LiScCl_6$, and $Cs_2LiInCl_6$ (hexagonal, 12L-type) were selected from pieces cut from big crystals under dry mineral oil and sealed into thin-walled glass capillaries. The quality of the crystals was checked by using film techniques. Complete intensity data sets were collected with a Siemens-Stoe four-circle diffractometer (AED 2). For details, see Tables I and II.

Samples suitable for optical spectroscopic measurements can easily be cleaved from the crystal boules. Their vanadium content was determined by atomic absorption analysis to be lower than 1% (mole) for all the samples investigated. The equipment and setups for the spectroscopic experiments are described in ref 6 and 15. It was not possible to obtain polarized luminescence spectra of V^{3+} in the uniaxial lattices due to imperfect crystal surfaces leading to almost complete depolarization. Therefore, only unpolarized spectra are shown. A highly sensitive Ge detector/preamplifier (ADC 403L, operated at 77 K) was used to detect V^{3+} luminescence from both chloride and bromide elpasolites. The detector response is flat in the wavelength region of interest; therefore, the spectra are uncorrected. To detect the luminescence from K_2NaScF_6:V^{3+}, a photomultiplier with S1 characteristic was used (Hamamatsu R316-02, cooled to 120 K). Its response drops by 35% between 960 and 1040 nm, and the low-energy part of the uncorrected spectrum is therefore slightly too weak.

Luminescence decay curves and time-resolved spectra were measured with the experimental techniques described in ref 6 and 15. The magnetic field dependence of the luminescence decay time was measured with the sample crystal cooled in a cryomagnet (Oxford Instruments SM4). The luminescence was excited with the second and third harmonic lines of a Nd:YAG laser (Quanta Ray DCR 3D), dispersed through a 0.25-m monochromator (Spex minimate), and detected with a Ge detector/preamplifier system (ADC 403HS, DC to 1-MHz frequency response). A digital storage oscilloscope (Tektronix 2430A) was used to average the time-dependent signal. Data acquisition was performed with a microcomputer (Tektronix 4052A).

3. Results

3.1. Crystal Structures. By and large, elpasolites A_2BMX_6 may be derived from closest packed AX_3 layers stacked, in the hexagonal setting, in the [00.1] direction. With a stacking sequence ...ABC... the highest symmetry can be achieved, resulting in the cubic face-centered space group $Fm3m$. The site symmetry of interstices between these layers is $m3m$ (O_h): B^+ and M^{3+} are octahedrally surrounded by X^-. The structures of the four cubic elpasolites, K_2NaScF_6, Cs_2LiYCl_6, Cs_2NaYCl_6, and Cs_2NaYBr_6, were refined in the course of this work. The results are summarized in Table I.

Like the perovskites, AMX_3, and depending upon the actual composition and temperature, cubic elpasolites may distort to lower symmetry structures, for example, to the tetragonal system. These distortions arise from concerted octahedral rotations and/or tilts in two or three dimensions. Second-order phase transitions accompany the transformation from the paraelastic ($Fm3m$) to the ferroelastic phase. Formation of twins and multiples is a necessary and unavoidable consequence when cubic face-centered crystals are cooled through the transition temperature. Fortunately, as was previously shown for the example of $Rb_2NaTmCl_6$,[8] these distortions affect the actual site symmetry of the $[MX_6]$ octahedron only very marginally. Therefore, the crystal structures of the tetragonal elpasolites $K_2LiScCl_6$ and Rb_2NaYCl_6 were not determined.

The broad structural variety of the elpasolites (as of the perovskites) is achieved not only by octahedral tilting, but, more interestingly, by different stacking sequences of the AX_3 layers. While the cubic closest packed sequence, ...ABC..., leads to all octahedra $[BX_6]$ and $[MX_6]$ sharing vertices, all the other stacking sequences necessarily lead to octahedra sharing faces as well. Only face-sharing octahedra are observed with the ...AB... sequence, i.e., with a hexagonal closest packing of AX_3 layers. This structure was first solved for Cs_2LiGaF_6.[16] It is named a 2L-type structure in ref 16 because two AX_3 (CsF_3) layers stacked in the [00.1] direction are needed for identity. The identity period is equal to the length of the crystallographic c axis. Note that six layers are needed for identity in the hexagonal setting of the cubic elpasolite. A structure refinement was attempted for the 2L-type $Cs_2LiScBr_6$. The diffractometer lattice constants ($a = 7.611$ (1) Å, $c = 6.502$ (1) Å) are similar to those determined previously from powder data.[9] The atomic parameters for Cs^+ and Br^- refined well (Cs^+ in 2d, Br^- in 6i with $x = 0.1610$ (3) in space group $P\bar{3}m1$). However, Li^+ and Sc^{3+} could be refined only by assuming statistical distribution over the 1a and 1b sites with R values of 16 (R) and 5.7% (R_w) for 209 observed reflections. Although this result is unsatisfactory, it does not affect the interpretation of the spectroscopic data for two reasons: first, Li^+ and Sc^{3+} have essentially identical ionic radii[17] (0.76 and 0.75 Å, respectively)

---

(13) Meyer, G. *Inorg. Synth.* **1983**, *22*, 10.

(14) Andrews, L. J.; McCollum, B. C.; Bartram, R. H. *AIP Conf. Proc.* **1986**, *146*, 227.

(15) Reber, Ch.; Güdel, H. U. *Inorg. Chem.* **1986**, *25*, 1196.

(16) Babel, D.; Haegele, R. *J. Solid State Chem.* **1976**, *18*, 39.

(17) Shannon, R. D. *Acta Crystallogr.* **1976**, *A32*, 751.

(18) Sheldrick, G. M. "SHEL-X 76: Program for Crystal Structure Determination", University of Cambridge, U.K., 1976.

(19) Cromer, D. T.; Mann, J. B. *Acta Crystallogr.* **1968**, *A24*, 321. Cromer, D. T.; Liberman, D. J. *J. Chem. Phys.* **1970**, *53*, 1891.

(20) Morss, L. R. *J. Inorg. Nucl. Chem.* **1974**, *36*, 3876.

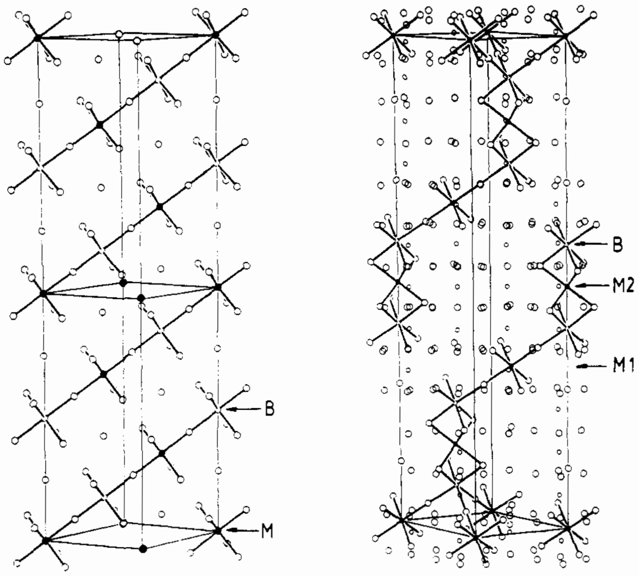

Figure 1. Perspective views of the crystal structures of the cubic face-centered elpasolite A_2BMX_6 (at left, two unit cells in the hexagonal setting) and of the 12L-type $Cs_2LiScCl_6$ (at right, the two inequivalent sites for M^{3+}, indicated as M1 and M2). Only a few of the vertex- and face-sharing octahedra are depicted for clarity.

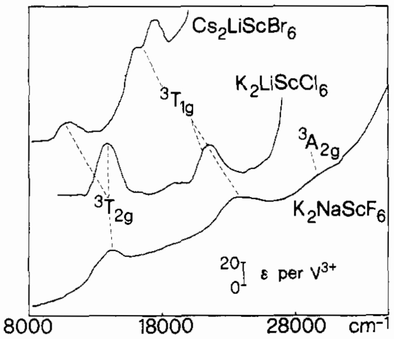

Figure 2. 20 K absorption spectra of V^{3+} in K_2NaScF_6, $K_2LiScCl_6$, and $Cs_2LiScBr_6$. The final states of the spin-allowed transitions in indicated (O_h notation).

and, second, they occupy trigonal antiprismatic sites of the same site symmetry ($\bar{3}m1$). The spectroscopically relevant result of the structure determination, i.e. the information on the trigonal elongation of the $[ScBr_6]$ octahedron, is not affected by the Li^+/Sc^{3+} disorder. $Sc^{3+}-Br^-$ distances are 2.673 Å (6×), and Br–Sc–Br angles are 86.87 (6×), 93.13 (6×) and 180° (3×).

Two (stacking) polytypes between ...ABC... and ...AB... have been observed for halide elpasolites.[10] One was first determined for 12L-type Cs_2NaCrF_6.[16] The stacking sequence is ...ABABCACABCBC... or $(chhc)_3$, space group $P\bar{3}m$. A perspective view of this structure (right-hand side) is compared with the cubic structure (left-hand side) in Figure 1. Twinning is also a problem for this structure type, and it was indeed observed with $Cs_2LiInCl_6$. As this crystal was judged to be a reverse–obverse twin with a 48:52 ratio of the two individuals, data sets for obverse and reverse reflections could be calculated by using a simple computer program.[22] Results of the refinement of the "obverse" individual are included in Table II and compared with the results of the refinement for $Cs_2LiScCl_6$, which originates from a data set recorded with an untwinned crystal. Pertinent distances and angles are summarized in Table II.

3.2. Optical Spectroscopy. The overall absorption spectra of V^{3+} doped into three representative fluoride, chloride, and bromide elpasolite lattices are shown in Figure 2. The broad bands are easily assigned to the spin-allowed transitions of a $(3d)^2$ system in O_h symmetry, as indicated in the figure. Corresponding bands are seen to suffer a greater red shift between the chloride and bromide than between the fluoride and chloride host. The splitting of the $^3T_{1g}{}^b$ band in $Cs_2LiScBr_6$ is the result of the D_{3d} (point symmetry of Sc^{3+} in that lattice.

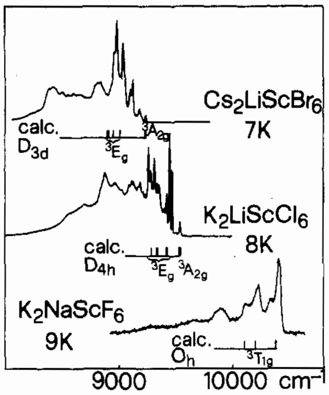

Figure 3. Low-temperature luminescence spectra of V^{3+} doped in $Cs_2LiScBr_6$, $K_2LiScCl_6$, and K_2NaScF_6. Calculated electronic splittings in the appropriate site symmetry are given below the experimental spectra.

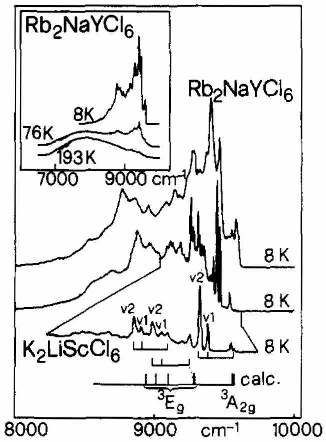

Figure 4. Low-temperature luminescence spectra of V^{3+} doped in two tetragonal chloride elpasolites, D_{4h} point symmetry. Calculated electronic splittings and assignments of electronic origins are included. Vibronic origins with the enabling modes v1 = 72 cm^{-1} and v2 = 95 cm^{-1} are designated. The insert shows the luminescence spectrum of $Rb_2NaYCl_6:V^{3+}$ at three temperatures.

Near-infrared luminescence is observed from all the hosts. In Figure 3 the low-temperature emission spectra are compared for the same three lattices as in absorption. The spectra are highly structured as expected for luminescence transitions originating in $^1T_{2g}$. Observed band positions are collected in Tables III and IV. An analysis of the fine structure in terms of electronic ground-state splittings and vibronic effects will be given in section 4.2. The variation in the widths of individual emission bands is very pronounced. For the highest energy transitions we estimate widths of 36, 10, and 12 cm^{-1} for the fluoride, chloride, and bromide lattices, respectively. These widths are inhomogeneous, and the fluoride crystal is obviously far from perfect, a finding which is in good agreement with the results of other fluoride crystals obtained with the Bridgman technique.[14] The observed red shift of the luminescence spectra between fluoride and bromide is interpreted in section 4.1.

Low-temperature luminescence spectra of two tetragonal chloride elpasolites are presented and compared in Figure 4. A slightly higher degree of inhomogeneity is observed in $Rb_2NaYCl_6:V^{3+}$ than in $K_2LiScCl_6:V^{3+}$, as can be recognized from the bandwidths. The crystal quality of these tetragonal lattices is deteriorated by phase transitions below the melting point, and it is therefore not astonishing to observe a broadening of the sharp luminescence transitions. There is a very strong similarity of the

---

(21) Simon, A. *J. Appl. Crystallogr.* **1970**, *3*, 11.
(22) Serafin, M. Universität Giessen, West Germany, unpublished work.
(23) Andrews, L. J.; Hitelman, S. M.; Kokta, M.; Gabbe, D. *J. Chem. Phys.* **1986**, *84*, 5229.

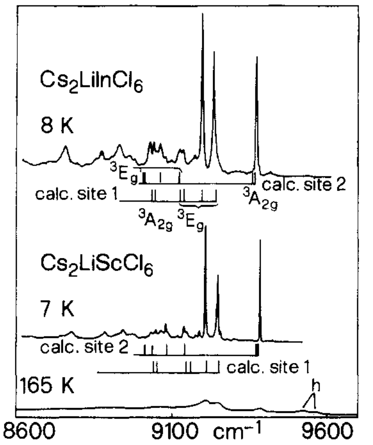

Figure 5. Low-temperature luminescence spectra of V^{3+} in two hexagonal chloride elpasolites. Calculated energy splittings and assignments of electronic origins of both crystallographic sites are shown.

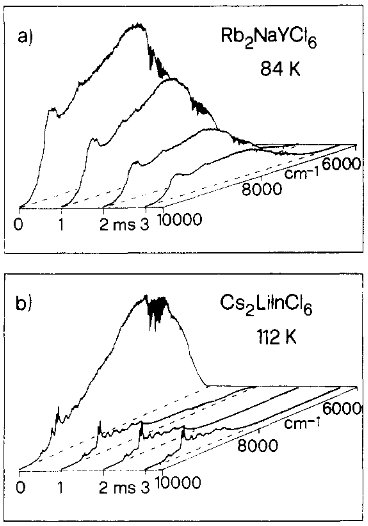

Figure 6. Time-resolved luminescence spectra of Rb_2NaYCl_6:V^{3+} (a) and $Cs_2LiInCl_6$:V^{3+} (b) at higher temperatures. The delay time after the exciting laser pulse is given on the abscissa (gate width for all the spectra 50 μs). The sharp negative features around 7000 cm^{-1} are due to atmospheric water absorptions.

two spectra with somewhat larger energy intervals between corresponding lines in Rb_2NaYCl_6:V^{3+}.

The temperature dependence of the luminescence spectrum is illustrated by Rb_2NaYCl_6:V^{3+} in the insert of Figure 4. The dramatic change from a sharp-line to a broad-band spectrum without any loss of total intensity is the result of a thermal population of the $^3T_{2g}$ excited state. It is observed for all the chloride and bromide lattices reported here, with a variation of the temperature interval in which it occurs, as discussed in section 4.3. From the broad-band $^3T_{2g} \rightarrow {}^3T_{1g}{}^a$ luminescence and the lowest energy $^3T_{1g}{}^a \rightarrow {}^3T_{2g}$ absorption maxima, the Stokes shift can be determined. All the resulting values are collected in the last column of Table V.

The best resolved luminescence spectra are those of the two hexagonal (12L) chloride lattices $Cs_2LiScCl_6$:V^{3+} and $Cs_2LiInCl_6$:V^{3+} shown in Figure 5. Both in their absolute energies and in their energy intervals between individual lines the two spectra are almost identical. The inhomogeneous broadening is slightly more pronounced for $Cs_2LiInCl_6$. Bandwidths of 10 and 7 cm^{-1} are estimated for the highest energy band in the indium and scandium lattices, respectively. The bottom trace in Figure 5 illustrates the occurrence of two sharp hot bands and the onset of broad-band luminescence from $Cs_2LiScCl_6$, two effects observed for $Cs_2LiInCl_6$ as well. Band positions in absorption and luminescence for all the lattices investigated are collected in Tables III and IV.

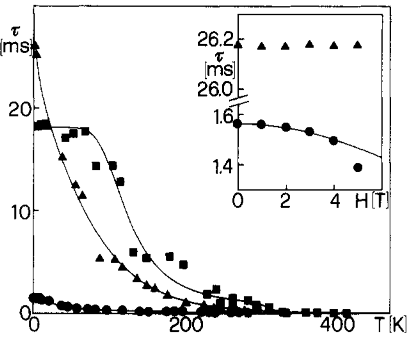

Figure 7. Temperature dependence of the luminescence decay times for V^{3+} in K_2NaScF_6 (triangles), $K_2LiScCl_6$ (squares), and $Cs_2LiScBr_6$ (circles). The solid lines in the main part are least-squares fits to eq 1 in ref 11. In the insert the 1.8 K luminescence decay times for the fluoride and bromide elpasolites are shown as a function of external magnetic field ($H \parallel c$ for $Cs_2LiScBr_6$:V^{3+}, arbitrary orientation for the cubic elpasolite K_2NaScF_6:V^{3+}). The solid curve for the bromide is a least-squares fit to eq 3.

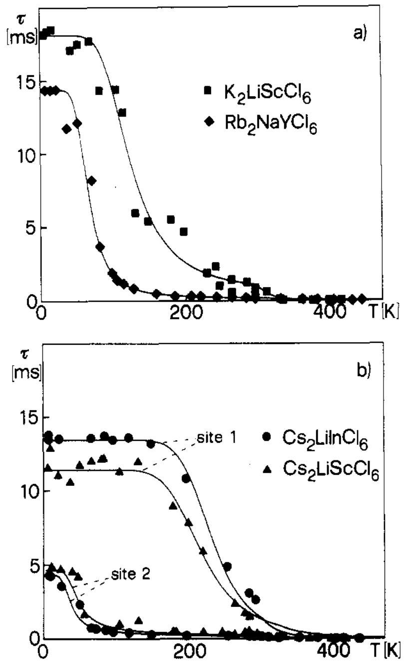

Figure 8. Temperature dependence of luminescence decay times for V^{3+} in tetragonal (a) and hexagonal (b) chloride elpasolites. The solid lines are least-squares fits to eq 1 in ref 11.

The time dependence after an excitation pulse of the V^{3+} luminescence spectra of Rb_2NaYCl_6 and $Cs_2LiInCl_6$ is presented in Figure 6. Without any quantitative analysis being discussed at this point, it is evident that the broad-band component in the 112 K spectrum of $Cs_2LiInCl_6$:V^{3+} decays almost completely within the first millisecond, while the sharp features at higher energy are still very strong after 3 ms. In Rb_2NaYCl_6 the broad and sharp spectral features decay with a much more similar rate. This is evidence for inequivalent luminophores in $Cs_2LiInCl_6$, and their relaxation behavior will be discussed in detail in section 4.2.

A quantitative handle on the relaxation properties is provided by luminescence decay time measurements. We found that all the decay curves were single exponentials within experimental accuracy. In Figure 7 a comparison is made of the luminescence decay times versus temperature for the same fluoride, chloride, and bromide elpasolites as in Figures 2 and 3. Imbedded in Figure 7 is the dependence of the 1.8 K decay time of K_2NaScF_6:V^{3+} and $Cs_2LiScBr_6$:V^{3+} on an external magnetic field. Decay times as a function of temperature for all the tetragonal and hexagonal chloride elpasolites are given in Figure 8. Pronounced differences in the relaxation behavior of the two sites in the hexagonal lattices of Figure 8b are evident from both the time-resolved spectra

Table II. $Cs_2LiScCl_6$ (Sc) and $Cs_2LiInCl_6$ (In): Crystallographic Data and Their Determination

crystal system trigonal; space group $R\bar{3}m$ (No. 166); $Z = 6$

lattice constants (in Å), molar volume V_m (in cm^3/mol), from Guinier–Simon[a] data

$Cs_2LiScCl_6$: $a = 7.2965\ (6)$, $c = 35.989\ (4)$, $c/a = 4.932$, $V_m = 166.56\ (4)$

$Cs_2LiInCl_6$: $a = 7.3184\ (4)$, $c = 36.240\ (3)$, $c/a = 4.952$, $V_m = 168.72\ (2)$

data collection: four-circle diffractometer Siemens-Stoe AED 2, Mo Kα radiation, graphite monochromator, $\lambda = 0.7107$ Å, ω (Sc)/ω–2θ (In) scan; scan speed and width: variable, $3° \leq \theta \leq 30/23.5°$, $F(000) = 1380/1584$, $\mu = 80.35/92.75\ cm^{-1}$ for Sc/In

data corrections: background, polarization and Lorentz factors; absorption: Sc, ψ-scan for 10 reflections, transmission factors ranging from 0.269 to 0.561

data statistics: Sc/In, 3457/5835 reflections collected (In, 1950 "obverse" reflections; see text), 661/361 unique reflections ($R_{int} = 0.052/0.066$), 652/358 with $|F_o| \geq 2\sigma|F_o|$

structure determination: program system SHEL-X 76,[b] structure factors from Cromer et al.,[c] initial atomic positions for Cs from Cs_2NaCrF_6[d] and for Cl, Sc/In, and Li from difference Fourier syntheses, full-matrix least-squares refinement, $R = 0.041/0.041$, $R_w = 0.035/0.052$; $w = k[\sigma(F_o)^2 + gF_o^2]^{-1}$ with $k = 0.052$, $g = 0$ and $k = 3.534$, $g = 0.21 \times 10^{-3}$.

Atomic Positions

		x/a	y/b	z/c	
Cs1	6c	0.0	0.0	0.126 36 (2)	Sc
				0.125 98 (4)	In
Cs2	6c	0.0	0.0	0.288 13 (2)	Sc
				0.289 18 (3)	In
Li	6c	0.0	0.0	0.408 9 (8)	Sc
				0.408 2 (12)	In
Sc1/In1	3a	0.0	0.0	0.0	
Sc2/In2	3b	0.0	0.0	0.5	
Cl1	18h	0.1569 (1)	$-x/a$	0.458 80 (5)	Sc
		0.1600 (2)		0.458 67 (7)	In
Cl2	18h	0.1724 (1)	$-x/a$	0.627 18 (5)	Sc
		0.1710 (2)		0.626 72 (8)	In

Temperature Factors: $\exp[-2\pi^2(U_{11}h^2a^{*2} + \ldots + 2U_{23}klb^*c^* + \ldots)]$ (U_{ij} in $Å^2$)

	U_{11}	U_{22}	U_{33}	U_{23}	U_{13}	U_{12}	
Cs1	0.0214 (3)	U_{11}	0.0235 (4)	0	0	$0.5U_{11}$	Sc
	0.0326 (7)		0.0253 (9)				In
Cs2	0.0210 (3)	U_{11}	0.0251 (5)	0	0	$0.5U_{11}$	Sc
	0.0320 (7)		0.0252 (9)				In
Li	0.0384 (99)	U_{11}	0.0330 (143)	0	0	$0.5U_{11}$	Sc
	0.0309 (122)		0.0454 (210)				In
Sc1	0.0112 (8)	U_{11}	0.0089 (13)	0	0	$0.5U_{11}$	
In1	0.0200 (7)		0.0087 (10)				
Sc2	0.0141 (9)	U_{11}	0.0088 (13)	0	0	$0.5U_{11}$	
In2	0.0242 (8)		0.0101 (10)				
Cl1	0.0242 (7)	U_{11}	0.0205 (8)	$-U_{13}$	0.0026 (3)	0.0150 (8)	Sc
	0.0367 (15)		0.0211 (18)		0.0022 (6)	0.0202 (14)	In
Cl2	0.0257 (7)	U_{11}	0.0243 (9)	0.0048 (4)	$-U_{23}$	0.0162 (8)	Sc
	0.0364 (16)		0.0244 (19)	0.0040 (6)		0.0216 (14)	In

Distances (Å) and Angles (deg) for $Cs_2LiScCl_6$/$Cs_2LiInCl_6$

Cs1–Cl1	3.650/3.660 (6×)	Cs2–Cl1	3.649/3.672 (3×)
Cs1–Cl1	3.685/3.696 (3×)	Cs2–Cl2	3.655/3.663 (6×)
Cs1–Cl2	3.730/3.736 (3×)	Cs2–Cl2	3.747/3.740 (3×)
Li–Cl2	2.536/2.510 (3×)		
Li–Cl1	2.675/2.731 (3×)		
Sc1/In1–Cl2	2.481/2.516 (6×)		
Cl2–Sc1/In1–Cl2	90.45/90.19 (6×)		
	89.55/89.81 (6×)		
	180 (3×)		
Sc2/In2–Cl1	2.476/2.521 (6×)		
Cl1–Sc2/In2–Cl1	92.17/91.68 (6×)		
	87.83/88.32 (6×)		
	180 (3×)		

[a] Reference 21. [b] Reference 18. [c] Reference 19. [d] Reference 16.

(Figure 6) and the decay time measurements. This will be correlated with structural results in section 4.2.

4. Discussion

4.1. Luminescence and Absorption Properties of V^{3+} in Fluoride, Chloride, and Bromide Host Lattices. In this section we give an overview and comparative discussion of the optical spectroscopic properties of V^{3+} in fluoride, chloride, and bromide elpasolites. We selected three hosts with Sc^{3+} as trivalent metal ion, i.e. K_2NaScF_6,[23] $K_2LiScCl_6$,[8] and $Cs_2LiScBr_6$.[9] Their crystal structures are cubic, tetragonal, and hexagonal, respectively. This choice is ideal for the illustration of the effects of both the chemical composition and the structure of the host lattice.

The V^{3+} ion has the [Ar]$3d^2$ electron configuration leading to four triplet states in O_h symmetry. The ground state is ${}^3T_{1g}{}^a$ (strong-field configuration $(t_{2g})^2$) and the excited triplet states are ${}^3T_{2g}$ $(t_{2g}e_g)$, ${}^3T_{1g}{}^b$ $(t_{2g}e_g)$, and ${}^3A_{2g}$ $(e_g)^2$. In addition to these triplet states there is a set of singlet excited states with ${}^1T_{2g}$ $(t_{2g})^2$ lowest in energy. In the absorption spectra of Figure 2 the spin-allowed triplet–triplet transitions are easily observed and assigned. The band positions for K_2NaScF_6:V^{3+} as shown in Figure 2 agree well with those reported for V^{3+} in a fluoride glass[24]

---

(24) Fonteneau, G.; Aliaga, N.; Corre, O.; Lucas, J. *Rev. Chim. Miner.* **1978**, *15*, 537.

Table III. Crystal-Field Parameters and Calculated and Observed Energy Levels (cm^{-1}) for V^{3+} Doped in Cubic Fluoride and Tetragonal Chloride Elpasolites

param/cm^{-1}	K_2NaScF_6	$K_2LiScCl_6$	Rb_2NaYCl_6	param/cm^{-1}	K_2NaScF_6	$K_2LiScCl_6$	Rb_2NaYCl_6
$10Dq$	15580	14300	12300	B	719	620	625
Ds	0	30	20	C	2790	2710	2710
Dt	0	−11	−20	ζ	124	88	110

O_h	spinor	calc	obs	D_{4h}	spinor	calc	obs	calc	obs
				$^3A_{2g}$	A_{1g}	0	0	0	0
$^3T_{1g}{}^a$	E_g	0	0		E_g	10	8	13	
	T_{2g}	2		^3E_g	B_{1g}	107	128	116	119
	T_{1g}	166	167		B_{2g}	108		118	
	A_{1g}	247	254		E_g	187	192	221	218
					A_{2g}	223	210	265	261
					A_{1g}	252	250	305	298
$^1T_{2g}$	T_{2g}	10 381	10 381	$^1B_{2g}$	B_{2g}	9 508	9 535	9 579	9 584
				^3E_g	B_{1g}	13 235		11 339	
					B_{2g}	13 245		11 355	
$^3T_{2g}$	A_{2g}	14 258			E_g	13 262		11 376	
	T_{2g}	14 294	14 230		A_{2g}	13 287	13 800	11 401	11 300
	T_{1g}	14 351			A_{1g}	13 287		11 402	
	E_g	14 352		$^3B_{2g}$	E_g	13 366		11 555	
					B_{1g}	13 370		11 557	
				^3E_g	A_{1g}	21 307		19 574	
					A_{2g}	21 312		19 618	
$^3T_{1g}{}^b$	A_{1g}	23 669			E_g	21 340		19 649	
	T_{1g}	23 711	23 720		B_{2g}	21 382	21 500	19 708	19 400
	T_{2g}	23 810			B_{1g}	21 383		19 711	
	E_g	23 813		$^3A_{2g}$	E_g	21 536		19 810	
					A_{1g}	21 543		19 814	
$^3A_{2g}$	T_{2g}	29 903	30 600						

Table IV. Crystal-Field Parameters and Calculated and Observed Energy Levels (cm^{-1}) for V^{3+} Doped in Hexagonal Chloride and Bromide Elpasolites

	$Cs_2LiScCl_6$		$Cs_2LiInCl_6$		
param/cm^{-1}	site 1[a]	site 2	site 1[a]	site 2	$Cs_2LiScBr_6$
$10Dq$	12850	12850	12800	12800	10850
$D\sigma$	81	−186	61	−188	−204
$D\tau$	−1	7	−1	8	11
B	628	647	624	645	626
C	2580	2568	2570	2572	2560
ζ	82	99	80	101	67

O_h	D_{3d}	spinor	calc	obs	calc	obs	calc	obs	calc	obs	calc	obs
$^3T_{1g}{}^a$	$^3A_{2g}$	A_{1g}	234	239	0	0	209	203	0	0	0	0
		E_g	209	203	8		177	173	8		5	
	^3E_g	E_g	0	0	233	243	0	0	229	236	222	222
		E_g	34	41	316	307	30	36	313	315	277	273
		A_{2g}	61	61	369	350	51	59	368	365	316	293
		A_{1g}	105	101	392	388	106	94	391	381	329	333
$^1T_{2g}$	^1E_g	E_g	9 242	9 248	9 386	9 386	9 236	9 233	9 376	9 375	9 236	9 237
$^3T_{2g}$	$^3A_{1g}$	A_{2g}	11 885		11 750		11 811		11 754		9 839	
		E_g	11 884		11 757		11 809		11 761		9 953	
	^3E_g	A_{1g}	11 735	12 600	11 981	12 600	11 688	11 800	11 984	11 800	10 085	10 300
		A_{2g}	11 744		11 982		11 698		11 985		10 098	
		E_g	11 759		12 007		11 713		12 012		10 106	
		E_g	11 779		12 030		11 734		12 035		10 120	
$^3T_{1g}{}^b$	$^3A_{2g}$	A_{1g}	20 224	20 200	20 135	20 200	20 082	19 900	20 110	19 900	17 911	17 500
		E_g	20 219		20 108		20 077		20 081		17 914	
	^3E_g	A_{1g}	19 972		20 599		19 879		20 575		18 510	
		A_{2g}	19 977	21 000	20 613	21 000	19 883	20 500	20 591	20 500	18 511	18 500
		E_g	20 000		20 642		19 906		20 620		18 840	
		E_g	20 038		20 679		19 945		20 658		18 567	

[a] Due to reversed trigonal splittings, observed and calculated energy levels for site 1 in $Cs_2LiScCl_6$ and $Cs_2LiInCl_6$ cannot be listed in increasing energy order.

and $[NH_4]_3[VF_6]$.[25] No splitting of the absorption bands is observed in the cubic K_2NaScF_6 and tetragonal $K_2LiScCl_6$ lattices. In contrast, the $^3T_{1g}{}^b$ absorption band of the hexagonal $Cs_2LiScBr_6$ shown in Figure 2 is clearly split into two components as a result of the D_{3d} point symmetry at the V^{3+} site. The comparison of the spin-allowed excitation energies for the three different halides is a nice illustration of the spectrochemical series;[26] i.e., the transition energies are highest for the fluoride and lowest for the bromide due to the decreasing ligand-field strength.

---

(25) Ballhausen, C. J.; Winther, F. *Acta Chem. Scand.* **1959**, *13*, 1729.

(26) Orgel, L. S. *An Introduction to Transition Metal Chemistry: Ligand Field Theory*, Methuen: London, 1960.

Table V. Radiative Relaxation Parameters for V^{3+} in All the Elpasolite Lattices Investigated

host	τ_S/ ms^a	g_S	τ_T/ μs^a	ΔE/ cm$^{-1\,a}$	$\hbar\omega_{\text{enabl}}$/ cm$^{-1\,b}$	Stokes shift/ cm^{-1}
K_2NaScF_6	26.1^d	3				
$K_2LiScCl_6$	18.1	1	374	421	297	2900
Rb_2NaYCl_6	14.4	1	181	272	198	3000
$Cs_2LiScCl_6$, site 1	11.4	2	296	891	310	3300
$Cs_2LiScCl_6$, site 2	4.6	2	210	145	310	3300
$Cs_2LiInCl_6$, site 1	13.5	2	232	923	202	3250
$Cs_2LiInCl$, site 2	4.3	2	186	119	202	3250
$Cs_2LiScBr_6$	1.5	2	272	61	120	3400

^{a} Determined from the fit of eq 1 in ref 11. ^{b} Determined from absorption spectra. ^{c} Determined from absorption and broad-band luminescence maxima. ^{d} Observed decay time at 1.8 K, which is shorter than τ_S due to nonradiative contributions.

A phenomenologically similar trend is observed in the luminescence spectra of V^{3+} in K_2NaScF_6, $K_2LiScCl_6$, and $Cs_2LiScBr_6$ (Figure 3). As in the case of the absorption spectra, the luminescence from the fluoride occurs higher in energy than that from the chloride and bromide lattices. Sharp-line luminescence from V^{3+} originates from the $^1T_{2g}$ excited state. It is therefore an intraconfigurational transition, similar to the well-known R lines observed in Cr^{3+} systems. In contrast to the case of the absorption spectra, the observed shifts of the luminescence spectra are due to differences in the interelectronic repulsion parameters. The nephelauxetic series[27] was introduced to account for such differences. The observed trend is as expected; i.e., the interelectronic repulsion parameters (Tables III and IV) and therefore the luminescence transition energies are largest for the fluoride and smallest for the bromide elpasolites. A quantitative interpretation of the nephelauxetic effect has been given by Jørgensen.[27] The nephelauxetic ratio β is factorized into a ligand and a metal contribution according to eq 2.[27] Values for h and k are tabulated

$$(1 - \beta) = h(\text{ligand})\, k(\text{metal}) \qquad (2)$$

in ref 27. For our V^{3+} luminescences we determined β as the ratio of the observed $^1T_{2g} \rightarrow {}^3T_{1g}{}^a$ transition energy and the energy of the ^1D term of the free V^{3+} ion.[28] The barycenter of all the observed electronic luminescence transitions was taken as the transition energy. The β values obtained by this procedure are symmetry-independent to a good approximation, reflecting only the effect of the chemically different environment. Their numerical values are 0.96, 0.89, and 0.86 for K_2NaScF_6, $K_2LiScCl_6$, and $Cs_2LiScBr_6$, respectively. The ratios of $(1 - \beta)$ for the three systems are independent of the metal ions and can be calculated from the h values in Jørgensen's table.[27] We obtain

calculated from ref 27	from experiment
$\dfrac{(1-\beta)_{6F^-}}{(1-\beta)_{6Cl^-}} = \dfrac{h(6F^-)}{h(6Cl^-)} = 0.40$	$\dfrac{(1-\beta(K_2NaScF_6))}{(1-\beta(K_2LiScCl_6))} = 0.36$
$\dfrac{(1-\beta)_{6Cl^-}}{(1-\beta)_{6Br^-}} = \dfrac{h(6Cl^-)}{h(6Br^-)} = 0.87$	$\dfrac{(1-\beta(K_2LiScCl_6))}{(1-\beta(Cs_2LiScBr_6))} = 0.79$

The agreement is remarkably good, and we can safely conclude that the nephelauxetic effect is mainly responsible for the observed shifts.

Other interesting properties to compare are the luminescence decay times presented in Figure 7. As expected for a spin- and parity-forbidden d–d transition, the low-temperature decay times are in the millisecond range, similar to those of the Cr^{3+} R lines. Again, a distinct trend is observed within the series of fluoride, chloride, and bromide host lattices: Low-temperature decay times are 26.1 (1.8), 18.1 (6), and 1.5 ms (8 K) for K_2NaScF_6, $K_2LiScCl_6$, and $Cs_2LiScBr_6$, respectively. The radiative decay time of the $^1T_{2g}$ excited state is determined by the amount of triplet character mixed into the $^1T_{2g}$ wave functions through spin–orbit coupling from the energetically close-lying $^3T_{2g}$ state. An important determinant for the amount of mixing is the energy difference between the two excited states.[29] This difference increases with ligand-field strength, and the amount of mixing therefore increases from fluoride to bromide, in agreement with the observed increase of the low-temperature decay rate.

According to ref 30 for a situation with a highly forbidden transition from the lowest energy excited state and an allowed transition from a nearby higher excited state, the radiative luminescence decay time depends on an external magnetic field as

$$\tau(H) = \tau(H = 0)/(aH^2 + 1) \qquad (3)$$

The magnitude of a is a measure of the mixing between singlet and triplet states by H. For $Cs_2LiScBr_6{:}V^{3+}$ the experimental values of τ vs H are shown in the insert of Figure 7. The fit of eq 3 to the data yields a value $a = 0.003\ T^{-2}$. The experimental values up to 4 T are nicely reproduced by eq 3. The deviation at 5 T may be due to a magnetic field induced change in the vibronic intensity mechanism of the $^3T_{2g} \rightarrow {}^3T_{1g}{}^a$ transition, not accounted for by eq 3. The fluoride decay times do not show any magnetic field dependence up to 5 T. We conclude that a is at least 1 order of magnitude smaller, mainly as a result of the larger energy difference between $^1T_{2g}$ and $^3T_{2g}$ in K_2NaScF_6 compared to $Cs_2LiScBr_6$. These experiments show very clearly that the effect of a physical perturbation such as an external magnetic field of 5 T on the radiative decay time is at least 1 order of magnitude smaller than the effects induced by chemical variation.

4.2. Correlation of Spectroscopy and Structure. a. Cubic and Tetragonal Elpasolite Lattices. The fine structure observed in all the low-temperature luminescence spectra presented in Figures 3–5 originates in both electronic and vibronic ground-state splittings. The following discussion strongly relies on a detailed analysis of the fine structure in the low-temperature V^{3+} luminescence spectrum of the cubic elpasolite Cs_2NaYCl_6 that was reported in ref 6. In O_h symmetry the $^3T_{1g}{}^a$ ground state is split by spin–orbit coupling into four spinor levels with E_g, T_{2g}, T_{1g}, and A_{1g} symmetry. In first order a Landé pattern is expected with the E_g and T_{2g} spinors degenerate and at lowest energy. The purely electronic transitions are forbidden for an electric dipole (ED) intensity mechanism, and the main intensity is expected in the vibronic sidebands. Therefore, electronic splittings as well as vibrational energies in the electronic ground state can be derived from luminescence spectra. For the calculation of electronic splittings we use the strong-field computational scheme outlined in ref 7. The crystal-field parameter $10Dq$ is adjusted to reproduce the absorption band positions. The remaining parameters are adjusted to reproduce the observed electronic transition energies in the low-temperature luminescence spectra. The results are collected in Tables III and IV.

From a comparison with the electronic ground-state splittings in the cubic elpasolite $Cs_2NaYCl_6{:}V^{3+}$, it is straightforward to assign the prominent sharp emission bands at high energy to electronic origins as indicated in Figure 3. The experimental transition energies can easily be reproduced with a crystal-field calculation. The Racah and spin–orbit parameters are reduced to 83 and 62% of their respective free-ion values. In contrast to the energy splittings the intensity distribution in the 9 K emission spectrum is not easily understood in terms of an O_h site. The origins are prominent, which is incompatible with a magnetic dipole (MD) intensity mechanism. There are three possible explanations for this: (i) the Sc^{3+} site in the host lattice is slightly noncentric despite the X-ray diffraction result that determines an exactly octahedral site; (ii) the V^{3+} ions substituting for Sc^{3+} occupy a slightly noncentric position in the lattice; (iii) there is a low-temperature phase transition to a noncentric structure, which is less likely than cases i and ii, since no change in the luminescence

---

(27) Jørgensen, C. K. *Prog. Inorg. Chem.* **1962**, *4*, 73.

(28) The ^1D energy of 10536 cm^{-1} was taken from: Bashkin, S.; Stoner, J. O. *Atomic Energy Levels and Grotrian Diagrams*; North Holland: Amsterdam, 1981; Vol. III.

(29) Walsh, C. G.; Donegan, J. F.; Glynn, T. J.; Morgan, G. P.; Imbusch, G. F.; Remeika, J. P. *J. Lumin.* **1988**, *40/41*, 103.

(30) Gliemann, G. *Comments Inorg. Chem.* **1986**, *5*, 263.

fine structure of V^{3+} is observed between 5 and 150 K. From a comparison of ionic radii,[17] 0.64 Å for V^{3+} and 0.75 Å for Sc^{3+}, we favor explanation ii. The electronic splittings resulting from this distortion are obviously smaller than the experimental bandwidths and thus not detectable. A set of vibrational sidebands is observed 560 cm^{-1} below the electronic origins, indicating the typical range of metal–ligand vibrational energies in the fluoride elpasolite.

The structural differences between the cubic and tetragonal chloride elpasolites are only small; nevertheless, the fine structure observed in the luminescence spectra of Rb_2NaYCl_6:V^{3+} and $K_2LiScCl_6$:V^{3+} (Figure 4) clearly reflects the influence of the tetragonal crystal-field component. The splitting pattern of the electronic origins is distinctly different from an O_h pattern, as can be seen from a detailed comparison with the cubic Cs_2NaYCl_6 spectrum. The enlarged fine structure of the highly resolved $K_2LiScCl_6$:V^{3+} spectrum at the bottom of Figure 4 is assigned in terms of electronic and vibronic origins. We notice that in contrast to the case for K_2NaScF_6:V^{3+} the most intense emission lines have vibronic origins with enabling modes in very similar, but tetragonally split, modes as in Cs_2NaYCl_6:V^{3+}. No detailed crystal structure information is available for the two tetragonal host lattices, but from their X-ray powder pattern they are reported to be isostructural to $Rb_2NaTmCl_6$.[8] This structure has two inequivalent Tm^{3+} sites with slightly different coordination geometries. The resolved fine structure on the high-energy side of the spectra in Figure 4 is well accounted for by only one V^{3+} site. This is supported by the time-resolved spectra in Figure 6a, which are typical of a one-site V^{3+} emission with some inhomogeneity in the site. We conclude that a D_{4h} site is preferentially occupied by V^{3+} in these lattices and analyze the fine structure and decay behavior accordingly. Good starting values for the crystal field parameters C, B, $10D_q$, and ζ were available from the cubic parent compound Cs_2NaYCl_6:V^{3+}. The tetragonal parameters[31] Ds and Dt were then adjusted to reproduce the observed line positions in Figure 4. Both Ds and Dt are very small, on the order of 0.2% of $10Dq$, indicating very small deviations from O_h symmetry. In both Rb_2NaYCl_6 and $K_2LiScCl_6$ the sign of the tetragonal distortion is such that it places the $^3A_{2g}$ component of $^3T_{1g}{}^a$ below the ^3E_g component. If the tetragonal component of the crystal field is due to a distortion of the VCl_6^{3-} units, it has to be tetragonally elongated to produce the above order of states. We can therefore use the high-resolution luminescence spectroscopy of V^{3+} as a very sensitive structural probe of the local site symmetry. Since the tetragonal field is very small, it is not reflected in the absorption spectra, and the Stokes shifts (Table V) are very similar to the value of 2970 cm^{-1} observed for the cubic Cs_2NaYCl_6 host.

b. Hexagonal Elpasolite Lattices. The two crystal structure types for hexagonal elpasolites were presented in section 3.1. We will first focus on the luminescence spectrum of $Cs_2LiScBr_6$:V^{3+}, the lattice with the 2L structure and one site for the trivalent metal ion. This is the first example of a $(3d)^2$ ion in a bromide environment that exhibits sharp-line emission at low temperatures. Both Ti^{2+} in $MgBr_2$[7] and V^{3+} in Cs_2NaYBr_6[6] show broad-band luminescence down to the lowest temperatures. We are obviously very close to the $^1T_{2g}/^3T_{2g}$ crossover point in this coordination, and very small variations in the host lattice may lead to a change of the emitting state. This was confirmed by high-pressure experiments on Cs_2NaYBr_6:V^{3+}, which showed the onset of some singlet emission at 26 kbar and 20 K. A chemical perturbation, however, is obviously much more effective than a pressure of 26 kbar to switch lowest excited states, as evidenced by the $Cs_2LiScBr_6$:V^{3+} spectrum.

An analysis and assignment of the fine structure in the $Cs_2LiScBr_6$:V^{3+} emission in terms of electronic splittings and vibronic sidebands is only possible by a comparison with the other host lattices discussed here and the cubic parent compound Cs_2NaYBr_6:V^{3+}. As in the case of the tetragonal systems treated in 4.2.a, the electronic origins are weaker than the vibronic origins, which is compatible with the D_{3d} point symmetry of the Sc^{3+} site in the host lattice. The result of a detailed analysis of the fine structure is given in Figure 3. The trigonal splitting of $^3T_{1g}{}^a$ has to be relatively large, i.e. of the order of a few hundred wavenumbers, to account for the observed pattern. The relatively weak highest energy peak is assigned to the two unresolved spinor components of $^3A_{2g}$. The four spinors arising from ^3E_g overlap with strong vibronic sidebands of $^3A_{2g}$. A crystal-field calculation was carried out with octahedral starting parameters from Cs_2NaYBr_6:V^{3+} and the trigonal parameters $D\sigma$ and $D\tau$ adjusted to fit the observed $^3T_{1g}{}^a$ splittings. $D\sigma$ and $D\tau$ are defined in ref 31, and their transformation to v,v' and K,K' trigonal parameters is given in ref 32. The experimental splittings are well reproduced with a $D\sigma$ parameter of the order of 2% of $10Dq$ for $Cs_2LiScBr_6$:V^{3+} (Table IV). This is 1 order of magnitude larger than the tetragonal parameters in the lattices discussed above. It indicates a stronger deviation from exactly octahedral symmetry in the present case.

Since we do have structural information for $Cs_2LiScBr_6$, a more detailed correlation between the $^3T_{1g}{}^a$ splitting and the geometry of the V^{3+} site can be made. According to the results presented in section 3.1 the angle α between the trigonal axis and the Sc–Br vector is 52.55° (ideal octahedron: 54.74°) and the Sc^{3+}–Br distance is 2.673 Å. The octahedral unit is therefore strongly elongated. A simple point charge calculation[33] of V^{3+} in this geometrical arrangement predicts the following trigonal splitting of t_{2g}: e_g 600 cm^{-1} below a_{1g}. This leads to a splitting of $^3T_{1g}{}^a$ with $^3A_{2g}$ lower than ^3E_g by 270 cm^{-1}, a splitting which corresponds exactly to the experimental difference between the barycenters of $^3A_{2g}$ and ^3E_g of 269 cm^{-1}, as determined from the observed spinor levels in Table IV. This extraordinary agreement between observed and calculated splittings is clearly fortuitous and can certainly not always be expected from the simple point charge model.

We now turn to the V^{3+}-doped hexagonal (12L) chloride elpasolites $Cs_2LiScCl_6$ and $Cs_2LiInCl_6$. Highly resolved, sharp luminescence spectra are observed from these systems at low temperatures (Figure 5). In addition they show a very interesting time dependence at higher temperatures (Figure 6b). This allows a more detailed data analysis. The very close similarity of the luminescence spectra in the two lattices indicates very similar crystallographic sites for V^{3+}. In contrast to those of the elpasolites discussed up to now, the luminescence spectra in Figure 5 cannot be rationalized "per se": it is not obvious at all whether the two distinctly different crystallographic sites for the trivalent metal ion derived in section 3.1 are reflected in the spectra or whether only one site is occupied by V^{3+}. The method of choice to separate transitions belonging to different sites is time-resolved luminescence spectroscopy. Two sites with significantly different coordination geometry should have a different luminescence decay behavior. In the present situation this can very nicely be exploited because the luminescence spectra change from long-lived sharp-line to short-lived broad-band spectra upon warming as a result of the $^3T_{2g}$ population. This change occurs below 100 K for site 2 in $Cs_2LiInCl_6$, while site 1 shows sharp-line luminescence up to 300 K. The time-resolved emission spectrum shown in Figure 6b illustrates this very clearly. The sharp-line luminescence at high energy, which is due mainly to site 1, decays 2 orders of magnitude slower than the broad-band emission at lower energy, which is due to site 2. Using the time and temperature dependence, it is thus straightforward to assign all the lines in the low-temperature emission spectrum to sites 1 and 2, as shown in Figure 5. According to the intensity distribution in Figure 5 the population of the two sites for V^{3+} is about equal; i.e., in contrast to the tetragonal lattices there is no evidence for a preference of one site. In the time-resolved spectrum 0 ms after the laser pulse at 112 K (Figure 6b), on the other hand, the broad emission from site 2 is about 2 orders of magnitude more intense that the sharp-line

---

(31) Ballhausen, C. J. *Introduction to Ligand Field Theory*, McGraw-Hill: New York, 1962.

(32) Perumareddi, J. R. *Phys. Status Solidi* **1973**, *B55*, K97.

(33) Double-ζ d orbitals were taken from: Clementi, E.; Roetti, C. *At. Data Nucl. Data Tables* **1974**, *14*, 177.

emission from site 1. The reason for this difference lies in the very nature of time-resolved spectra: the measured intensity ratios are determined by the populations and the decay times of the two sites, and thus, integration over time is necessary to obtain correct intensity ratios.

In both host lattices and for both sites the pure electronic origins are dominant in intensity. This is hard to reconcile with the D_{3d} point symmetry of both trivalent sites in the 12L structure. A noncentric contribution to the crystal-field potential at the V^{3+} sites is likely. From a comparison of ionic radii,[17] 0.64, 0.75, and 0.80 Å for V^{3+}, Sc^{3+}, and In^{3+}, respectively, it is conceivable that the V^{3+} ions are slightly displaced off the center of the D_{3d} site. The two sites have distinctly different electronic splitting patterns, as illustrated in Figure 5. In site 1 the trigonal splitting is smaller and of opposite sign to site 2. Both splittings are well reproduced by crystal-field calculations with the parameters given in Table IV. The site 2 splitting is comparable in sign and magnitude to the splitting found for $Cs_2LiScBr_6:V^{3+}$. As in the latter system it is possible to correlate the splittings with the coordination geometry.

Inspection of the structural data in Table II shows that one of the sites is elongated along the trigonal axis (site 2, $\alpha = 53.27$ and 53.54° for $Cs_2LiScCl_6$ and $Cs_2LiInCl_6$, respectively), the other is slightly compressed (site 1, $\alpha = 55.03$ and 54.87° for $Cs_2LiScCl_6$ and $Cs_2LiInCl_6$, respectively). As in $Cs_2LiScBr_6:V^{3+}$ the relatively large trigonal splitting with $^3A_{2g}$ lower in energy corresponds to the elongated site 2, where the other splitting pattern is due to the slightly compressed octahedron of site 1. Point charge calculations were done for these lattices with the same model as described for $Cs_2LiScBr_6:V^{3+}$. For site 2 the trigonal t_{2g} splitting is as follows: e_g below a_{1g} by 470 and 361 cm^{-1} in $Cs_2LiScCl_6:V^{3+}$ and $Cs_2LiInCl_6:V^{3+}$, respectively. This leads to stabilization of $^3A_{2g}$ with respect to ^3E_g of 233 and 176 cm^{-1} for the Sc^{3+} and the In^{3+} elpasolites, respectively. Again, the comparison with the experimental splittings (Table IV) of 306 and 308 cm^{-1} is good regarding the simplicity of the model. For site 1 ^3E_g is calculated to be stabilized with respect to $^3A_{2g}$ by 42 and 20 cm^{-1} in $Cs_2LiScCl_6:V^{3+}$ and $Cs_2LiInCl_6:V^{3+}$, respectively. The agreement with the experimental values of 174 and 145 cm^{-1}, respectively, is only qualitative in this case.

From the remarkable correlation of $^3T_{1g}{}^a$ splittings and the $MX_6{}^{3-}$ geometry of the host in all the hexagonal lattices studied here, we conclude that the trigonal splitting in these elpasolites is caused by distortions of the first-coordination sphere.

In halide lattices such as $CsMgCl_3$ or $MgCl_2$ with pronounced one-dimensional or two-dimensional character we found that divalent transition-metal ions substituting for Mg^{2+} experience low-symmetry crystal fields that are strongly determined by the nearest-neighbor cations in the lattice. The $MCl_6{}^{4-}$ distortions account for only a small fraction of the low-symmetry crystal-field potential in these anisotropic lattices. This is in contrast to the elpasolite lattices discussed here, in which the contribution of the nearest cations to the crystal field is isotropic, and thus the low-symmetry potential is determined by the $MX_6{}^{3-}$ distortions.

Our high-resolution luminescence spectra clearly indicate that in some cases the V^{3+} site symmetry is lower than the site symmetry of the pure host lattice determined by X-ray diffraction. A noncentric component of the crystal-field potential provides electric dipole intensity to the purely electronic origins in nominally centrosymmetric sites. In other lattices, on the other hand, the pure origins do have the small oscillator strengths expected for ED forbidden transitions. The conclusion is that we have an intrinsically rather flat potential with respect to at least one of the enabling modes, and a very small perturbation then leads to an equilibrium position which is slightly off-center.

4.3. Radiative and Nonradiative Relaxation. Information about radiative and nonradiative relaxation processes is contained in the temperature dependence of the luminescence decay times (Figures 7 and 8) and the time-resolved spectra in Figure 6. Detailed accounts of the theoretical models have been given elsewhere. In ref 6 the relaxation behavior of $Cs_2NaYCl_6:V^{3+}$ was discussed in detail both in the radiative and nonradiative temperature regimes. In ref 11 the nonradiative relaxation of V^{3+} in a variety of crystal lattices was discussed in terms of its dependence on chemical and structural variation. Here we analyze and discuss the radiative relaxations in the whole series of elpasolite lattices and establish some correlations with the structural and spectroscopic properties. The relevant factors in the nonradiative processes are briefly summarized.

The luminescence decay times versus temperature allow a quantitative determination of the energy separation ΔE between the singlet and triplet excited states as well as the individual radiative decay times of these two states. If the model outlined in detail in ref 6 is used, the temperature dependence of the radiative decay time τ_{rad} is given by

$$\tau_{rad} = [\tau_S{}^{-1}P_S + \tau_T{}^{-1}P_T \coth(\hbar\omega_{enabl}/2kT)]^{-1} \qquad (4)$$

$$P_S = g_S/Z$$

$$P_T = 9[\exp(-\Delta E/kT)]/Z$$

$$Z = g_S + 9\exp(-\Delta E/kT)$$

with τ_S and τ_T denoting the radiative decay times for the singlet and triplet excited states with Boltzmann populations P_S and P_T, respectively. g_S is the degeneracy of the lowest singlet excited state. A possible splitting of $^3T_{2g}$, which is known to be small, is neglected. Also neglected are any other singlet states in this energy range. The coth term describes the increase of the radiative $^3T_{2g} \rightarrow {}^3T_{1g}{}^a$ rate due to the vibronic intensity mechanism. The value for the enabling mode $\hbar\omega_{enabl}$ was determined from the temperature dependence of the corresponding absorption transition.[34] τ_S was kept constant at the experimental low-temperature decay time. The two adjustable parameters in this radiative model are therefore ΔE, the energy difference between the singlet and triplet excited state potential minima, and τ_T, the radiative decay time of the triplet excited state. The parameter values obtained from least-squares fits to the data are collected in Table V. ΔE values range from 61 to 923 cm^{-1}. There is a clear correlation of ΔE with the geometrical distortion of the octahedral site. This is most pronounced for the two inequivalent sites in the 12L lattices $Cs_2LiScCl_6$ and $Cs_2LiInCl_6$. In both of them site 1 has a ΔE of approximately 900 cm^{-1}, whereas the corresponding value for site 2 is less than 150 cm^{-1}. The strong trigonal crystal-field potential at site 2 pushes the $^3A_{2g}$ component of $^3T_{2g}$ to lower energy, thus decreasing ΔE. This is paralleled by the singlet lieftimes τ_S, which are approximately three times bigger for site 1 than for site 2. We can easily rationalize this as follows: τ_S is determined by the triplet character mixed into the singlet state through spin–orbit coupling. $^3T_{2g}$ is the main source of triplet character, and with increasing ΔE the mixing gets weaker as observed. A low-energy $^3T_{2g}$ component is also the likely reason why $Cs_2LiScBr_6:V^{3+}$ has a ΔE value of only 61 cm^{-1}, comparable to the values for the geometrically similar site 2 in the 12L chloride lattices. In contrast to $Cs_2NaYBr_6:V^{3+}$ the scandium bromide elpasolite is a singlet emitter, most likely due to the stronger ligand field caused by the shorter M^{3+}–Br^- distance: 2.673 Å in $Cs_2LiScBr_6$ versus 2.765 Å in Cs_2NaYBr_6. We here use the same "hole size" argument as for the tetragonal lattices $K_2LiScCl_6$ and Rb_2NaYCl_6 in section 4.2.a.

This radiative decay model accounts for the temperature dependence of τ in the bromide and chloride lattices below 250 K. A second drop, which is now accompanied by a corresponding drop of the luminescence intensity, occurs between 250 and 350 K. Detailed experimental data for all the lattices reported here and their interpretation in terms of nonradiative relaxation processes were given in ref 11. The solid curves in Figures 7 and 8 correspond to least-squares fits in which both radiative and nonradiative effects were taken into account: eq 1 in ref 11.

Among all the elpasolite lattices $K_2NaScF_6:V^{3+}$ displays quite an exceptional behavior. Nonradiative relaxation contributes to the luminescence decay time down to 1.8 K; it has thus a much lower quenching temperature than any of the chloride and bromide

---

[34] Ferguson, J. *Prog. Inorg. Chem.* **1970**, *12*, 262.

3258 *Inorg. Chem.* **1989**, *28*, 3258-3262

lattices. The nonradiative decay rates depend on both the chemical composition and the site geometry of the host lattice. Chemical variation has a bigger effect than structural variation. The observed decrease of the quenching temperature in the series chloride, fluoride, oxide can be simply explained by the energy gap law:[35] The number of vibrational quanta p needed to bridge the energy gap between the emitting state and the ground state decreases in this series as a result of increasing vibrational energies. A quantitative discussion of this dependence on the parameter p is given in ref 11. The degree of distortion at the V^{3+} site is mainly responsible for the variations observed within the chloride elpasolite lattices in Figures 7 and 8. We found that this distortion is also reflected in the Huang–Rhys parameter S, and the quenching temperatures could be correlated with S.[11]

In conclusion we find that by variation of the chemical composition and the site symmetry and geometry of V^{3+} in a number of elpasolite host lattices we obtain a great deal of insight into the nature of the first excited states, the radiative and nonradiative relaxation processes. This insight cannot be obtained by the study of one compound alone, the trends within the series being very important for spectroscopic assignments as well as a physical understanding of the effects. High-resolution optical luminescence spectroscopy in the near-IR region at low temperatures with its extremely high information content is an essential experimental technique for the study of V^{3+} and Ti^{2+} ions.

Acknowledgment. We are grateful to Prof. R. Hoppe and Dr. F. Averdunk, Universität Giessen, West Germany, for their help with the synthesis of the fluoride elpasolite, to Dr. M. Serafin, Universität Giessen, for help with crystallographic calculations, and to G. Koch for his continuous help in the preparation and preliminary investigation of single crystals for X-ray diffraction. Financial support of this work by the Swiss National Science Foundation and the Fonds der Chemischen Industrie, West Germany, is gratefully acknowledged.

---

(35) Moos, H. W. *J. Lumin.* **1970**, *1/2*, 106.

Contribution from the Department of Electronic Chemistry, Tokyo Institute of Technology at Nagatsuta, Midori-ku, Yokohama 227, Japan, and Coordination Chemistry Laboratories, Institute for Molecular Science, Myodaiji, Okazaki 444, Japan

Formation of Binary and Ternary Complexes of Cadmium(II) with Halide Ions and 2,2′-Bipyridine in *N*,*N*-Dimethylformamide

Shin-ichi Ishiguro,*[†] Kazuhiko Ozutsumi,[†] Makoto Miyauchi,[†] and Hitoshi Ohtaki[‡]

Received February 22, 1989

The formation of binary and ternary complexes of cadmium(II) with halide ions (X) and 2,2′-bipyridine (bpy) has been studied by calorimetry in *N*,*N*-dimethylformamide (DMF) containing 0.1 mol dm^{-3} $(C_2H_5)_4NClO_4$ as an ionic medium at 25 °C. The formation of ternary $[CdX(bpy)]^+$, $[CdX_2(bpy)]$, $[CdX_3(bpy)]^-$, $[CdX(bpy)_2]^+$, and $[CdX_2(bpy)_2]$ complexes is proposed, together with binary halogeno $[CdX_n]^{(2-n)+}$ (n = 1–4; X = Cl, Br, I) and 2,2′-bipyridine $[Cd(bpy)_n]^{2+}$ (n = 1–3) ones, and their formation constants, enthalpies, and entropies are obtained. The coordination geometry is suggested to be six-coordination for $[CdX(DMF)_5]^+$ and four-coordination for $[CdX_2(DMF)_2]$, $[CdX_3(DMF)]^-$, and $[CdX_4]^{2-}$; i.e., the change from octahedral to tetrahedral occurs at the formation of $[CdX_2]$. The ternary complexes are six-coordinated, except for $[CdX_3(bpy)]^-$, which is five-coordinated. The $[CdX_3(bpy)]^-$ complex is formed as the dominant species in the chloride and bromide systems, while the formation of the corresponding iodide complex is practically negligible. Affinities of halide ions with Cd^{2+}, $[Cd(bpy)]^{2+}$, or $[Cd(bpy)_2]^{2+}$ are compared in view of the effect of bound 2,2′-bipyridine molecules on the Cd^{II}–X interactions.

Introduction

A number of studies have been carried out so far on the complexation of cadmium(II) with halide ions in not only water but also nonaqueous solvents,[1-8] and the formation of a series of mononuclear $[CdX]^+$, $[CdX_2]$, $[CdX_3]^-$, and $[CdX_4]^{2-}$ complexes has been elucidated. The coordination geometry of the solvated cadmium(II) ion in water,[9,10] dimethyl sulfoxide (DMSO),[11] and *N*,*N*-dimethylformamide (DMF),[12] which is octahedral with six solvent molecules solvating the central metal ion through oxygen atoms, has been established by X-ray diffraction. The coordination geometry in solution may be essentially the same as that in the crystal, as in the case for DMSO.[13] With the $[CdX_n]^{(2-n)+}$ complexes, the $[CdI_4]^{2-}$ geometry of an almost regular tetrahedron has been revealed by X-ray diffraction in water[14] and DMSO.[15] Also, six-coordination for $[CdI(H_2O)_5]^+$ and $[CdI(DMSO)_5]^+$ and four-coordination for $[CdI_3(DMSO)]^-$ have been revealed in relevant solutions.[16] Ahrland discussed the variation of thermodynamic parameters of the formation of $[CdX_n]^{(2-n)+}$ (n = 1–4) in water and DMSO in relation to changes in their coordination structure,[2] suggesting that the change from octahedral to tetrahedral occurs at the formation of $[CdX_3]^-$ in water but at the formation of $[CdX_2]$ in DMSO. It is also noteworthy that the log K_1 value of $[CdX]^+$ increases in the order Cl < Br < I in water, while the reverse is the case in DMSO.[2] With regard to the relative order of stabilities an extended work including fluoride ion has recently been made in some binary solvent mixtures.[8]

We have so far reported ternary complexation equilibria of the divalent transition-metal ions[17-19] Cu^{2+}, Zn^{2+}, and Ni^{2+}, using

---

[†] Tokyo Institute of Technology.
[‡] Institute for Molecular Science.

(1) Högfeldt, E. *Stability Constants of Metal-Ion Complexes*; IUPAC Chemical Data Series 21; Pergamon Press: Oxford, England, 1982; Part A (Inorganic Ligands).
(2) Ahrland, S. *Pure Appl. Chem.* **1979**, *51*, 2019.
(3) Ahrland, S.; Björk, N.-O. *Acta Chem. Scand., Ser. A* **1976**, *30*, 249.
(4) Ahrland, S.; Björk, N.-O. *Acta Chem. Scand., Ser. A* **1976**, *30*, 257.
(5) Ahrland, S.; Björk, N.-O.; Persson, I. *Acta Chem. Scand., Ser. A* **1981**, *35*, 67.
(6) Ahrland, S.; Persson, I. *Acta Chem. Scand., Ser. A* **1981**, *35*, 185.
(7) Ackerman, J. J. H.; Orr, T. V.; Bartuska, V. J.; Maciel, G. E. *J. Am. Chem. Soc.* **1979**, *101*, 341.
(8) Bixler, J. W.; Cobb, M. E.; French, R. J.; Morse, B. E.; O'Toole, T. R.; Schudel, J. A.; Yogis, G. A.; Bond, A. M. *Inorg. Chim. Acta* **1987**, *128*, 105.
(9) Bol, W.; Gerrits, G. J. A.; van Panthaleon van Eck, C. L. *J. Appl. Crystallogr.* **1970**, *3*, 486.
(10) Ohtaki, H.; Maeda, M.; Itoh, S. *Bull. Chem. Soc. Jpn.* **1974**, *47*, 2217.
(11) Sandström, M.; Persson, I.; Ahrland, S. *Acta Chem. Scand., Ser. A* **1978**, *32*, 607.
(12) Ozutsumi, K.; Takamuku, T.; Ishiguro, S.; Ohtaki, H. *Bull. Chem. Soc. Jpn.* **1989**, *62*, 1875.
(13) Tsurumi, M.; Maeda, M.; Ohtaki, H. *Denki Kagaku oyobi Kogyo Butsuri Kagaku* **1977**, *45*, 367.
(14) Pocev, S.; Triolo, R.; Johansson, G. *Acta Chem. Scand., Ser. A* **1979**, *33*, 179.
(15) Sandström, M. *Acta Chem. Scand., Ser. A* **1978**, *32*, 519.
(16) Ohtaki, H.; Johansson, G. *Pure Appl. Chem.* **1981**, *53*, 1357.
(17) Ishiguro, S.; Nagy, L.; Ohtaki, H. *Bull. Chem. Soc. Jpn.* **1987**, *60*, 2053.
(18) Ishiguro, S.; Nagy, L.; Ohtaki, H. *Bull. Chem. Soc. Jpn.* **1987**, *60*, 2865.